H-Dibaryon Search in the Reaction $\Xi^- d \rightarrow Hn$ at Rest by Measuring the Neutron in Coincidence with the Ξ^-

By

Toru IIJIMA*

Department of Physics, Faculty of Science, Kyoto University
Kyoto 606-01, Japan

(Received December 19, 1994)

Abstract

An experiment to search for the $S = -2$ H dibaryon with Ξ^- atomic-capture reactions in liquid deuterium has been carried out at the Brookhaven 2-GeV/c kaon beam line. By using a specialized target of liquid hydrogen and deuterium, Ξ^- hyperons created with $K^- p \rightarrow K^+ \Xi^-$ reactions are slowed down in a degrader and are brought to rest in liquid deuterium. Silicon detectors placed between the hydrogen and deuterium targets provide the tagging of stopping Ξ^-'s based on the energy loss measurement. The signature of the H is a detection of monoenergetic neutrons from the $(\Xi^-, d)_{atom} \rightarrow Hn$ reaction in coincidence with the tagging signal. In this paper, the method and technique used in the experiment are described and the results obtained from the first data collected in 1992 are presented. It is shown that the present experiment is an effective approach to search for the H particle.

1. Introduction

The H particle is a six-quark state (q^6) with the flavor-singlet configuration of *uuddss*, $I = 0$ and $J^\pi = 0^+$, which was first predicted by Jaffe in 1977 using the MIT bag model [1]. He showed that the mass would be 2150 MeV, about 80 MeV below the $\Lambda\Lambda$ threshold at 2231 MeV, and therefore the state would be stable against strong decay. Since then, the H mass (m_H) has been estimated in a variety of calculations such as the bag model [2, 3, 4, 5], quark cluster models [6, 7, 8, 9] and lattice QCD [10, 11, 12]. The predicted m_H ranges from two-nucleon mass ($2m_N$) to two-lambda mass ($2m_\Lambda$) and also beyond $2m_\Lambda$. Several experimental efforts have been made to search for this object. However, no conclusive evidence has been found so far [13, 14, 15, 16]. A number of events have been reported as H candidates in photographs of a propane bubble chamber exposed to a 10-GeV/c proton beam [17, 18, 19], however, interpretations of the events are controversial [20]. Double hypernuclei which have been found in nuclear emulsion [21, 22, 23] may exclude deeply bound H's, however, they do not exclude H's with binding energy up to a few tens of MeV or unbound H's. Therefore, both theoretical and experimental situations regarding the existence of the H remain unsettled.

A search for the H in Ξ^- atomic-capture reactions in liquid deuterium has been carried out at the Brookhaven AGS [24]. In this experiment, two successive reactions

---

* Present address: National Laboratory for High Energy Physics, Tsukuba 305, Japan.

$$K^- + p \rightarrow K^+ + \Xi^- \tag{1}$$

$$(\Xi^-, d)_{atom} \rightarrow H + n, \tag{2}$$

where $(\Xi^-, d)_{atom}$ denotes a $\Xi^- d$ atom, have been studied. Ξ^- hyperons are created by the double strangeness exchange $K^- p \rightarrow K^+ \Xi^-$ reactions in a liquid hydrogen target, are slowed down in a tungsten degrader and then are brought to rest in liquid deuterium. The stopped Ξ^-'s form bound atomic systems $(\Xi^-, d)_{atoms}$. If the neutron produced in the final state is detected, the reaction is kinematically determined and H is observed as a monoenergetic peak in the missing-mass spectra. The H mass is determined from the measured neutron energy. The same technique is applicable for unbound H's, which may exist as a resonance of $\Lambda\Lambda$ as suggested in Ref. [6]. In this case, the signal neutrons appear as a bump in the neutron energy spectrum whose width shows the resonance width.

The rate of the H production is evaluated by the branching ratio R for the $(\Xi^-, d)_{atom} \rightarrow Hn$ reaction which is given as

$$R = \Gamma_{\Xi^- d \rightarrow Hn} / \Gamma_{tot}$$
$$\Gamma_{tot} = \Gamma_{\Xi^- d \rightarrow Hn} + \Gamma_{\Xi^- d \rightarrow \Lambda\Lambda n} + \Gamma_{\Xi^- d \rightarrow \Xi^0 nn} + \Gamma_{\Xi^- d \rightarrow \gamma\Xi^- d} + \Gamma_{\Xi^- d \rightarrow \Lambda\pi^- d}. \tag{3}$$

Here the partial widths for possible processes from $(\Xi^-, d)_{atoms}$ such as the reactions $\Xi^- d \rightarrow \Lambda\Lambda n$ and $\Xi^- d \rightarrow \Xi^0 nn$, the radiative transition of the Ξ^- to other orbits $\Xi^- d \rightarrow \gamma\Xi^- d$ and Ξ^- weak decay $\Xi^- d \rightarrow \Lambda\pi^- d$ are shown as Γ's with suffixes. According to the calculation of Aerts and Dover, R for the Ξ^- capture from the S orbits is as large as 0.8 for the binding energy B_H close to zero and decreases with increasing B_H ($B_H = 2m_\Lambda - m_H$) [25][1]. It is expected, therefore, the measurement has higher sensitivity in the region of small B_H. This is the region where the above mentioned double hypernuclei do not exclude the existence of the H and also many theoretical calculations predict the m_H. No other experiment has explored this region with enough sensitivity.

In the reaction $(\Xi^-, d)_{atom} \rightarrow Hn$, the underlying process for the H production is the fusion reaction $\Xi^- p \rightarrow H$. In Ξ^--capture reactions at rest, the relative momentum of the initial two baryons is small, and ideal conditions to maximize the H-production rate are realized. An alternative approach to produce the H with the same process $\Xi^- p \rightarrow H$ is to use the (K^-, K^+) reaction on nuclear targets. When the Ξ^- produced by the (K^-, K^+) reaction collides with nucleons in the target nucleus, the Fermi motion of the nucleons provides a region of phase space where the relative momentum of a $\Xi^- p$ pair is small enough to produce the H directly. The direct production of the H has been studied with an emulsion target [16] and the H production with ^3He target, $K^- {}^3He \rightarrow K^+ Hn$, is in progress [26, 27]. However, the search around the $\Lambda\Lambda$ threshold with the direct process is difficult because of large background from the quasifree Ξ^- production.

To accomplish the H search in the two successive reactions, it is indispensable to

---

[1] Note that the partial widths for the radiative transition $\Gamma_{\Xi^- d \rightarrow \gamma\Xi^- d}$ and the Ξ^- weak decay $\Gamma_{\Xi^- d \rightarrow \Lambda\pi^- d}$ are also included in the definition of R in the present work. The weak decay width $\Gamma_{\Xi^- d \rightarrow \Lambda\pi^- d}$ is not included in the calculation of Aerts and Dover.

produce copious Ξ^-'s and discriminate them from other particles. In this experiment, a magnetic spectrometer instrumented with drift chambers, time-of-flight counters and Čerenkov counters is used for identification of K^+ produced in $K^-p \to K^+\Xi^-$ reactions. The liquid deuterium target for atomic capture of Ξ^-'s is installed on top of the hydrogen target for Ξ^- production. Tungsten degrader walls placed between the two targets are equipped with silicon detectors for the measurement of energy of Ξ^-'s which stop in liquid deuterium. Neutrons produced in the capture reactions are detected in coincidence with the tagged Ξ^-'s. The measurement of neutrons rather than decay products of *H* gives the sensitivity independent of the decay mode or life time of the *H*. This is a salient feature contrast to experiments searching for specific decay mode of *H* such as $H \to \Sigma^- p$ and $H \to \Lambda p \pi^-$, where the sensitivity is limited by fiducial volume of apparatus. The *H* search based on the atomic-capture process in liquid deuterium has not been previously carried out because of the lack of beam line to produce enough number of $(\Xi^-, d)_{atoms}$. The newly-built 2-GeV/c kaon beam line at the BNL-AGS has been successfully commissioned and it provides 1.8-GeV/c negative kaons with a flux of $1 \sim 2 \times 10^6$/spill. Hereby the *H* particle search with the Ξ^- capture process $(\Xi^-, d)_{atom} \to Hn$ has become possible.

The purpose of this paper is to demonstrate the effectiveness of the present measurement to search for the *H* particle. The technique used in the experiment are described and results obtained from the first data collected in 1992 are presented. Section 2 shows the experimental setup. In Section 3, we describe the method for the identification of the Ξ^- production with the spectrometer and the tagging of $(\Xi^-, d)_{atom}$ formation with the silicon detector. The resolution and background in the neutron detection are also explained. In Section 4, the neutron spectrum is examined to demonstrate the peak search procedure and the method of deducing an upper limit on the *H* production. Finally, the work is concluded in Section 5.

2. Experiment

2.1 Overview

The experiment was executed using the 2-GeV/c kaon beam line at the Brookhaven National Laboratory Alternating Gradient Synchrotron (BNL-AGS). Figure 1 shows a schematic layout of the experiment which involves 1) a magnetic spectrometer to identify the reaction $K^-p \to K^+\Xi^-$, 2) a double target of liquid hydrogen and deuterium (LH_2/LD_2 target) for the formation of $(\Xi^-, d)_{atom}$ and 3) a neutron detection system to measure the signal neutrons from the reaction $(\Xi^-, d)_{atom} \to Hn$.

The kaon beam line delivered 1.8-GeV/c K^- mesons to create Ξ^- hyperons with $K^-p \to K^+\Xi^-$ reactions in liquid hydrogen filled in the lower half of the LH_2/LD_2 target, which is shown in Figure 2. In the beam line, three scintillator hodoscopes (MP, MT and IT), an aerogel Čerenkov counter (IC) and three drift chambers (ID1-3) were installed for identification and tracking of the K^- beam. The outgoing K^+ was analyzed with a magnetic spectrometer placed downstream the target. The magnetic field was 1.4 Tesla at the center of a dipole magnet (48D48). The field direction was horizontal and thus outgoing particles were bent vertically. The K^+ was identified by
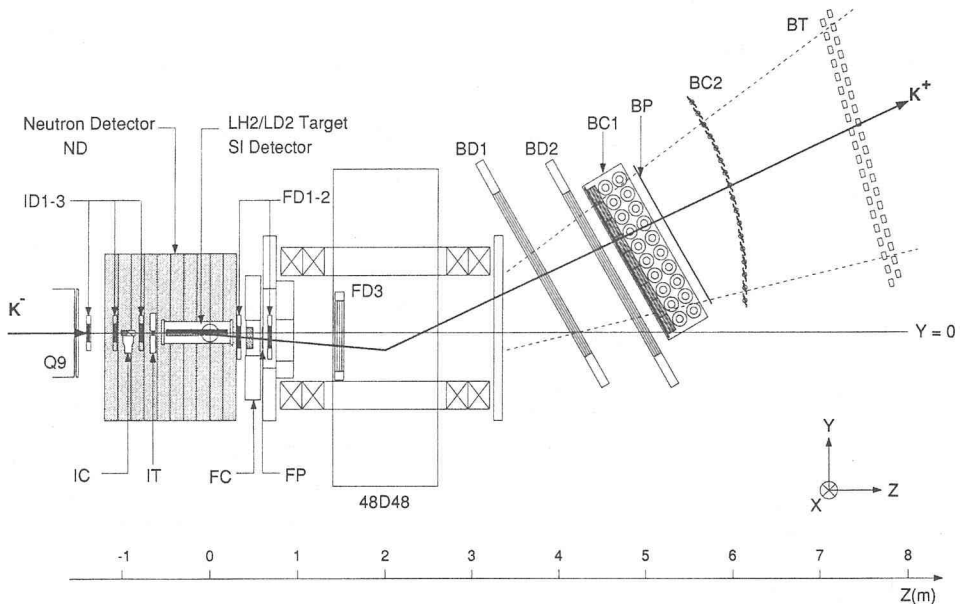
Fig. 1. Schematic side view of the experimental setup. The beam line
hodoscopes MP and MT are shown in Figure 3.

the measured momentum and velocity calculated from the time-of-flight (TOF) data
and the path length.   The momentum was derived from the trajectory which was
reconstructed with five drift chambers (FD1-3 and BD1-2).   The TOF information was
obtained from data on a time-of-flight array (BT) which was installed at the end of the
spectrometer.   Background particles in the K^+ identification were mainly pions and
protons.   Two aerogel Cerenkov counters (FC and BC1) differentiated the K^+ from
the π^+, whereas a lucite Cerenkov counter (BC2) was used to reduce the protons, which
dominated in the outgoing channel.   Two scintillator hodoscopes (FP and BP) were
used to form a primary on-line trigger.

The LH_2/LD_2 target system was the heart of the experimental setup.   The target
was featured by twenty tungsten degrader wedges which were installed on top of the
LH_2 vessel, as shown in Figure 2.   The Ξ^- was emitted at an angle of about $18°$, while
the K^+ was detected by the spectrometer at an angle of about $8°$.   The created Ξ^- left
the LH_2 vessel, passed through one of the degrading cells and then entered the LD_2
vessel with the velocity low enough to stop in liquid deuterium.   Even with this
specialized target geometry, the fraction of Ξ^-'s stopping in LD_2 was very small
(0.24%).   The vast majority of Ξ^-'s decayed in flight or stopped in degraders to result
in giving background neutrons.   Another important information on stopping Ξ^-'s
came from pads of silicon detectors (SI) mounted behind each degrader wedge.   A
large pulse in one of the pads near the production vertex was an indication of a Ξ^-
which was slow enough to stop in the LD_2 vessel.   The tagging of stopping Ξ^-'s with
the silicon detector was one of keys to improve the ratio of signal neutrons to
background neutrons.

Another major equipment for the experiment was a neutron detection system (ND)
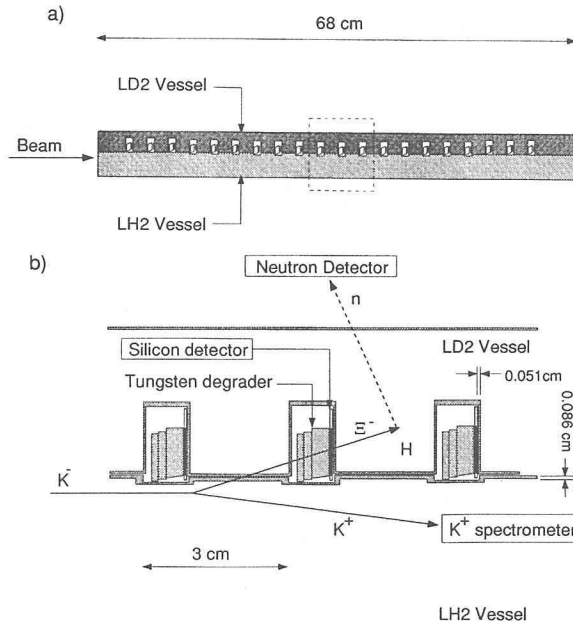
Fig. 2.   a) Side view of the LH_2/LD_2 target.   b) Close-up of Ξ^- degrader cells.

to measure signal neutrons from the *H* formation, $(\Xi^-, d)_{atom} \rightarrow Hn$. Two arrays of scintillator logs (LN and RN) surrounded the target to measure the time-of-flight of neutrons. Therefore, the signal of the *H* formation $(\Xi^-, d)_{atom} \rightarrow Hn$ was a peak observed in the neutron TOF (or velocity) spectrum.

2.2   2-GeV/c Kaon Beam Line

The newly-built 2-GeV/c kaon beam line delivers high intensity K^- beams of the order of 10^6/spill. Details of the beam line are described in Ref. [28]. For better separation between kaons and other particles such as pions, the beam line features two stages of velocity selection and magnetic optics corrected to third order. Figure 3 shows a schematic layout of the beam line. Primary protons accelerated to 24 GeV/c by the AGS are incident on a 9 cm-thick platinum target located at the entrance of the first dipole (D1). Secondary particles are transported with extraction angle of 5° and a momentum acceptance of $\pm 3\%$ (FWHM). After the velocity is selected with two stages of separators (CM1-E1-CM2 and CM3-E2-CM4), they are delivered to the final focus point (FF). In Table 1 are summarized the design parameters of the beam line.

The beam line has been operational since 1991. A K^- flux of about 2.3×10^6 per 10^{13} protons and a π^-/K^- ratio of lower than 0.8 have been achieved at 1.8 GeV/c with the two separators running at 750 KV (E1) and 600 KV (E2) and the mass slit openings set to 1.9 mm (MS1) and 2.8 mm (MS2)[2].

---

[2] These results were obtained in the 1993 run. In the 1992 run, the K^- flux was about 2.8×10^6 per 10^{13} protons and π^-/K^- ratio was about 2.5 : 1 with the separators running at 750 KV (E1) and 375 KV (E2) and with the mass slit openings set to 3.5 mm (MS1) and 3.9 mm (MS2). In the 1993 run, the beam purity was improved in trade for some loss in the K^- flux compared to the 1992 run.
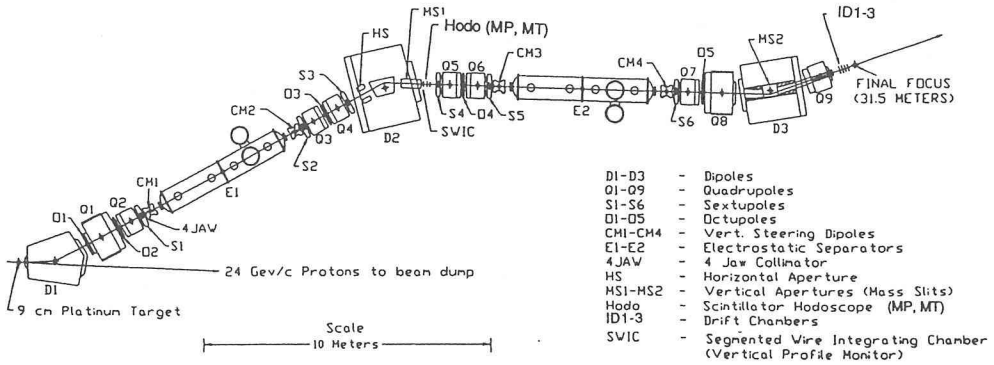
T. IIJIMA

Fig. 3. Schematic layout of the BNL-AGS 2-GeV/c K^- beam line.

Table 1. Design parameters of the AGS 2-GeV/c kaon beam line.

Momentum range	up to $2\,\mathrm{GeV}/c$
Production target (length×width×height)	$9.0\times0.7\times1.0\,\mathrm{cm}^3$
Central production angle	$5°$
Momentum acceptance (FWHM)	$\pm3\%$
Separators (E1 and E2)	750 KV 4.5 m long (each), 10 cm gap
Solid angle-momentum acceptance[a]	6.2–6.5 msr % (MS1=3 mm, MS2=4 mm)
Length	31.4 m

[a] calculated with the RAYTRACE program.

To minimize the flight path length of $\varXi^-$'s between their production points and the LD_2 target and thus to minimize the rate of $\varXi^-$ decay in flight, a well defined beam with a small vertical width must be delivered to the position near the top of the LH_2 target.
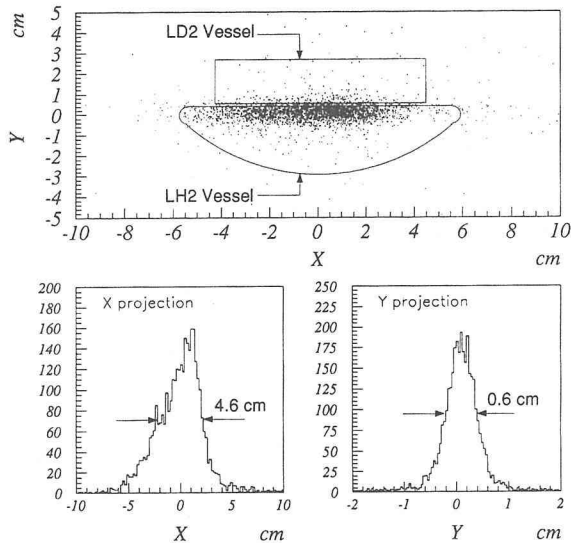

Fig. 4. Profile of the K^- beam at the final focus point. The beam is positioned at near top of the LH_2 vessel.

For this purpose the last quadrupole Q9 is designed to focus the beam in the vertical direction. Figure 4 shows the beam profile on the final focal plane which is reconstructed with drift chambers ID1-3. The size of the K^- beam (FWHM) has been measured to be 0.6 cm in the vertical direction and 4.6 cm in the horizontal.

2.3 Spectrometer Devices
2.3.1 Scintilldtor Hodoscopes

In Table 2 are summarized the specifications of five scintillator hodoscopes, MP, MT, IT, FP and BP. The hodoscopes MP and MT were installed downstream the first mass slit MS1 (see Figure 3). The primary function of MP was the determination of the beam momentum by measuring the x-position of the particle, whereas that of MT is the measurement of the time-of-flight of the beam in comparison to IT. The hodoscope IT with the intrinsic timing resolution of 60 psec (σ) provided the reference timing signal (START) for all the detectors. The hodoscopes FP and BP defined the spectrometer acceptance. For particles produced at the target center, the out-of-beam elements (#1-#12) of FP gave a vertical angular coverage of $-13.2° \leq \theta_Y \leq 0.6°$, whereas BP gave a horizontal coverage of $|\theta_X| \leq 6.4°$. Most of the beam hit the module #13 of FP, and the top four elements (#13-#16) of FP were used as beam vetoes.

Table 2. Specifications of the scintillator hodoscopes. The orientation is indicated by the direction of hodoscope slats (V : vertical, H : horizontal).

Hodoscope	Orientation	Dimension of one element[a]	Segmentation
MP	V	1.5× 0.7×0.3	9
MT	V	1.5× 3.7×0.6	72
IT	V	3.0× 2.5×1.3	4
FP	H	24.0× 1.5×0.4	16
BP	V	180.0×21.0×1.0	6

[a] length×width×thickness (cm^3)

2.3.2 Drift Chambers (ID1-3, FD1-3, BD1-2)

The spectrometer was instrumented with three drift chambers (ID1-3) to measure the track of an incident beam particle and five drift chambers (FD1-3 and BD1-2) to reconstruct the track of an outgoing particle through the magnet. The three beam drift chambers ID1-3 were identical and so were FD1 and FD2. The drift cell of these chambers were designed for operation at a high beam rate. Sense wires were positioned with a 5.1 mm (0.2″) spacing and thus the maximum drift distance was 2.5 mm, giving the maximum drift time of 50 nsec. The chamber FD3 was installed inside the magnet for better determination of the momentum. It provided fast outputs of y hits for a second-level trigger, which is described later. The chambers BD1 and BD2 had the active area of 124 cm × 224 cm. They had a similar design of drift cells with sense wires placed with 2.0 cm spacing. The position resolutions (σ) of these drift chambers were 0.2 mm for ID1-3 and FD1-2, 0.3 mm for FD3 and 0.4 mm for BD1-2.

2.3.3 Aerogel Čerenkov Counters (IC, FC, BC1)

In order to separate K^-'s from π^-'s in the 1.8-GeV/c beam, the aerogel Čerenkov counter IC with a refractive index (n) of 1.03 was used.   For the separation of outgoing K^+'s from π^+'s, two aerogel Čerenkov counters FC and BC1, both with n of 1.04, were installed in the spectrometer.   The function of BC1, located downstream the magnet, was not only the rejection of π^+'s produced in the target but also the rejection of background pions, muons and electrons originating from in-flight decay of incident K^-'s and also from secondary interactions of non-interacting beams or outgoing particles.
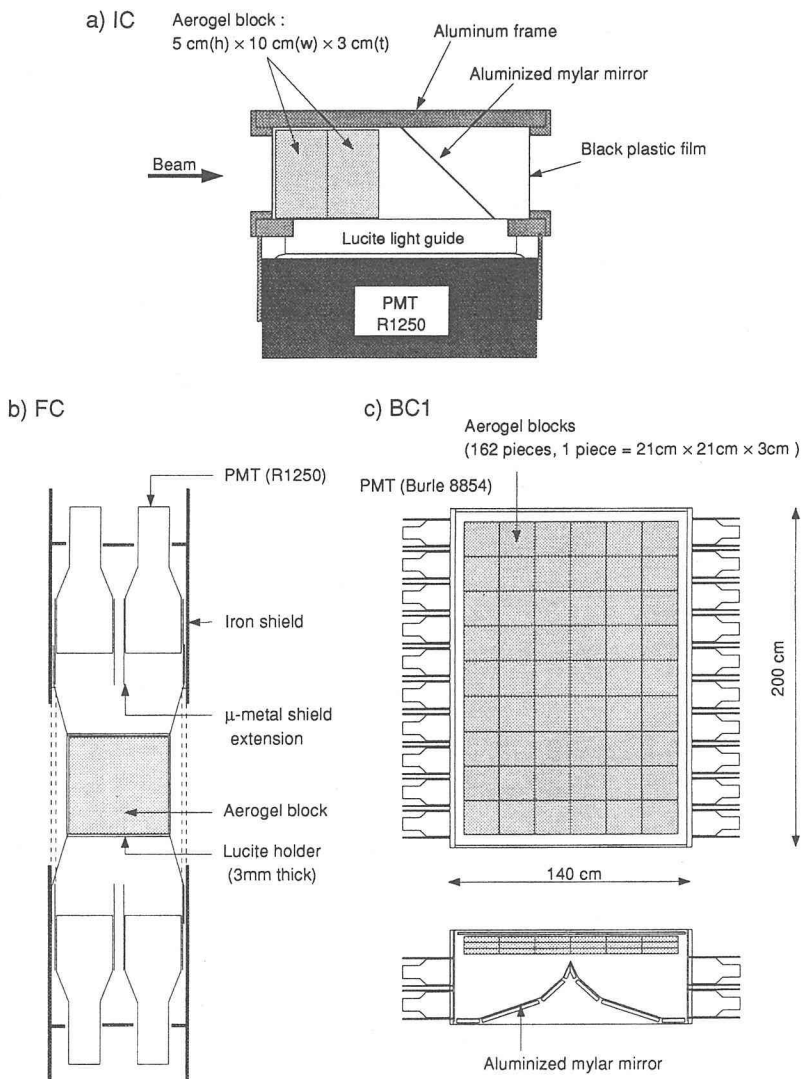
Fig. 5.   Schematic drawings for aerogel Čerenkov counters a) IC, b) FC and
c) BC1.

Table 3. Design parameters of aerogel Čerenkov counters

	IC	FC	BC1
Effective area (X×Y, cm²)	10×5	25×25	126×189
Total thickness (cm)	6.0	9.0	9.0
Dimension of a block (X×Y×Z, cm³)	10×5×3	25×25×3	21×21×3
Number of block	2	3	162 (=6×9×3)
Refractive index (n)	1.03	1.04	1.04
Threshold momentum for π/K (GeV/c)	0.56/1.97	0.49/1.74	0.49/1.74
Photomultiplier	Hamamatsu R1250	Hamamatsu R1250	Burle 8854
Number of channel	1	4	40

Figure 5 shows schematic drawings for IC, FC and BC1. In Table 3 is summarized the specifications of each counter. The aerogel blocks used for all of the devices were manufactured by the Airglass Company in Sweden. The radiator cells of these devices were coated with highly reflective white paper (Millipore) to prevent absorption of Čerenkov light. In the radiator cell of IC, a mirror of aluminized mylar was placed downstream the aerogel blocks to reflect the Čerenkov light emitted forward to a PMT. As for FC, the radiator cell was viewed by four PMT's through 30 cm-long air light guide coated with aluminized mylar. The counter BC1, with the effective area of 126 cm×169 cm effective area, was equipped with a mirror of aluminized mylar arranged in parabolic shape and was viewed by 40 PMT's. For detecting Čerenkov photons, PMT's with diameter of 5″ sensitive to a single photo-electron, Hamamatsu R1250 (IC and FC) and Burle 8854 (BC1), were used. The average numbers of photo-electron for 1.8-GeV/c pions were measured to be 5.8 for IC, 4.3 for FC and 4.2 for BC1.

2.3.4 Lucite Čerenkov Counter (BC2)

In the reactions induced by 1.8-GeV/c K^-'s on the proton target, K^+ is a rare particle comparing to π^+ and p which are produced by reactions such as $K^- p \to \pi^+ \Sigma^-$ and $K^- p \to pK^- (K^{*-})$. In particular, the ratio of protons to kaons in the outgoing channel is as large as 300. The lucite Čerenkov counter BC2 was installed for discrimination of K^+ from the proton, which was crucial to reduce the on-line trigger rate to an acceptable level for the data acquisition. The principle of the device is based on the mechanism of total reflection of the Čerenkov light. Consider a flat plate of lucite with refractive index of n placed orthogonal to the direction of a particle moving with velocity β. For sufficiently high β, the Čerenkov angle θ_c is large enough for total reflection of the light on the surface of the plate. Consequently, the light is detected with a photomultiplier installed at the end of the plate. On the other hand, the light produced by a slow particle is partially reflected and escapes the lucite plate after reflections of a few times. The Čerenkov angle θ_c and the critical angle for total reflection $\theta_{crit.}$ are given by:

$$\theta_c = \cos^{-1}(1/\beta n) \tag{4}$$

$$\theta_{crit.} = \sin^{-1}(n_0/n), \tag{5}$$

where n_0 is the refractive index of the medium outside the plate. Therefore, the
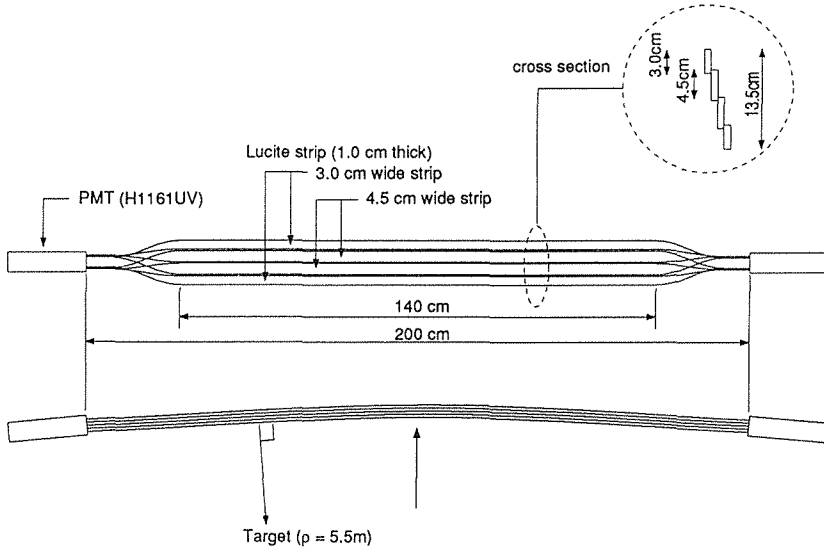
Fig. 6.   Design of one module of the lucite Čerenkov counter BC2.

threshold velocity β_{th} for total reflection is given by:

$$\beta_{th} = \frac{1}{\sqrt{(n^2 - n_0^2)}}.$$ (6)

If lucite with $n = 1.49$ is placed in air, Eq. (6) gives $\beta_{th} = 0.905$, corresponding to the momentum of 1.05 GeV/c for the K^+ and 2.0 GeV/c for the proton.

Figure 6 shows the design of one module of the device.   Each module consisted of four 1.0-cm thick strips of UV transparent lucite piled stepwise with 0.5-cm overlap. The four strips were gathered at the end of the module and coupled to a photomultiplier with an UV transparent window.   Since the device was highly sensitive to the incident
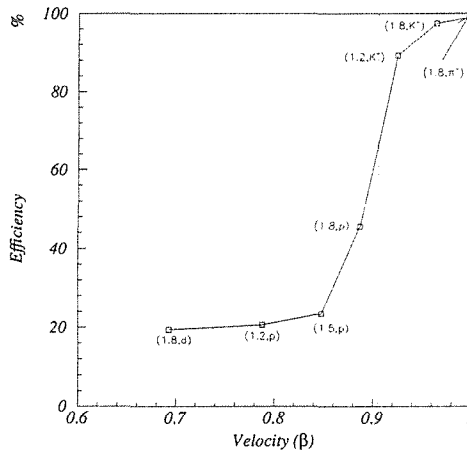

Fig. 7.   Measured response of BC2 to the particle velocity.   Dotted line indicates the designed threshold at $\beta = 0.905$.   The momentum and the particle species used for the measurement are shown in parenthesis for each point.

angle of particles, the module had a curvature of 5 m so that direction of all the particles from the target were nearly orthogonal to the lucite surface.

In Figure 7, the detection efficiency of the device is shown as a function of the particle velocity. It is shown that the efficiency increases rapidly around the designed threshold velocity (β_{th}=0.905). The efficiency for K^+ detection in the momentum region of interest, that is around 1.25 GeV/c, is about 90%. The remaining efficiency of about 20% in the velocity region far below the threshold arises from scintillating contaminant in lucite or the δ-ray emission. The on-line trigger rate was reduced down to about 30% using this device.

2.3.5 Time-of-flight Array (BT)

The time-of-flight array BT was located at the end of the spectrometer to measure TOF's of outgoing particles. The typical flight length was 7.9 m from the target, giving TOF difference of 1.8 nsec between the K^+ and π^+ with the momentum of 1.25 GeV/c. Details of the design and the device performance are described in Ref. [29]. The array consisted of 40 logs of plastic scintillators (BC408), each having a dimension of 200.0 cm long, 8.5 cm wide and 5.0 cm thick. Each end was directly coupled to a Hamamatsu H1949 PMT at each end. The signal from each anode was discriminated with a CFD (constant fraction discriminator, Phillips 715). Discriminated timing signals were then read by Kinetic F432 FASTBUS TDC and also by LeCroy FERA/FERET system to provide a fast conversion of signals for the second-level trigger. The TOF resolution averaged over 40 elements was found to be 130 psec (σ). By unfolding the resolution of the START signal (60 psec), the intrinsic timing resolution of 110 psec (σ) was obtained.

2.4 LH₂/LD₂ Target System

2.4.1 Ξ^- Degrader Cell

The Ξ^- degrader cells, which are shown in Figure 2-b), were designed to maximize the probability of Ξ^-'s stopping in LD_2. The degrader wedges, each having the thickness of 0.57 cm, were positioned every 3 cm on top of the 68 cm long LH_2 vessel. The geometry of wedge degraders had several advantages over a naive flat degrader plate sandwiched between the LH_2 and LD_2 vessels. First, the wedge geometry reduced a required active silicon detector area by a factor of 3. Secondly, the silicon detector pads were perpendicular to the beam halo instead of parallel. Thirdly, a practical design required to place the silicon detector pads in a gap between the degrader and the LD_2 vessel. In the flat geometry, a small increase of the gap would reduce the Ξ^- stopping efficiency significantly, because the Ξ^-'s passes through the gap in almost parallel. Finally, in the case that the silicon detectors and degraders were nearly perpendicular to the Ξ^- track, the angular correction to the energy loss in these material was minimized. In order to reduce the fraction of Ξ^-'s decaying in flight or stopping before entering into the LD_2 vessel, the thickness of aluminum walls of the target vessels had to be minimized. As indicated in Figure 2, the LD_2 vessel was machined so that the thickness of the aluminum wall where Ξ^-'s pass through is 0.05 cm, while the top plate of the LH_2 vessel had to be kept 0.086 cm thick to retain the mechanical strength.

2.4.2 Silicon Detector (SI)

The diffused junction silicon detectors were operated in vacuum at liquid hydrogen temperature ($\sim$20 K). Two silicon detector wafers, each having four pads with active area of 1 cm$\times$1 cm , were mounted on an aluminum-oxide ceramic frame, as shown in Figure 8. Twenty of such detectors were mounted in the Ξ^- degrader cells. Thus the total number of channel was 160. The thickness of each wafer was about 200 μm to give an energy deposit of about 70 KeV for minimum ionizing particles. The energy deposit of interest for Ξ^-'s stopping in LD_2, that is from 1.0 to 2.1 MeV as shown below, was 15 to 30 times higher than that for minimum ionizing particles.

2.4.3 Monte Carlo Simulation

The technique to tag the Ξ^-'s stopping in $LD_2^\prime$ has been tested with a Monte Carlo simulation. Figure 9-a) shows the stopping positions of Ξ^-'s created with the $K^- p \rightarrow K^+ \Xi^-$ reaction. It is seen that the fraction of Ξ^-'s stopping in LD_2 is very small
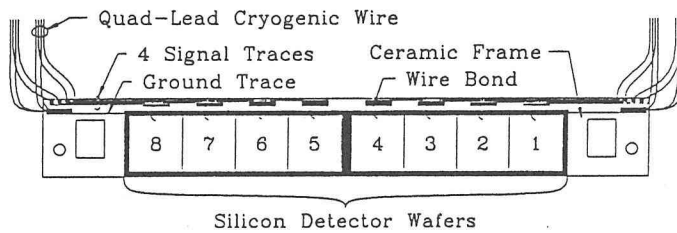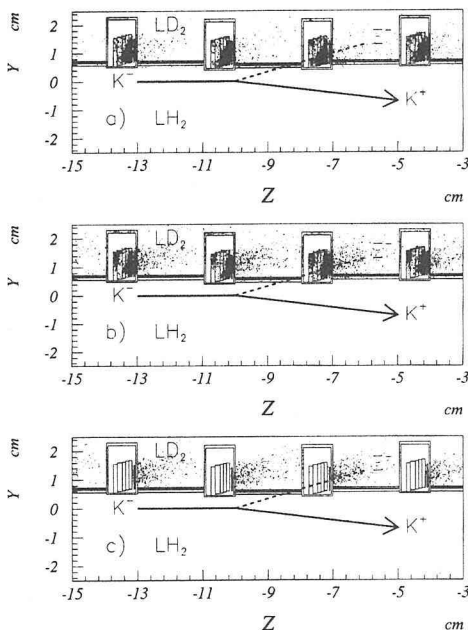

Fig. 8. Schematic layout of a silicon detector unit.

Fig. 9. Stopping positions of Ξ^-'s. Cuts applied are a) no cut, b) $5° \leq \theta_{K^+} \leq 9°$ and c) $5° \leq \theta_{K^+} \leq 9°$ and $1.0 \leq \Delta E_{SI}$ (MeV)$\leq$2.1
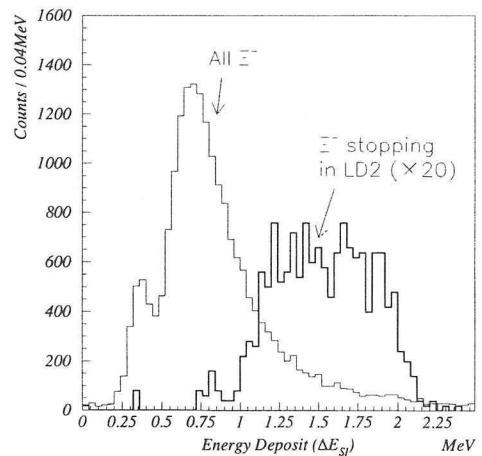
Fig. 10. Simulated energy deposit ΔE_{SI} for Ξ^-'s. Thick solid line shows the distribution for Ξ^-'s stopping in LD_2.

compared to those in degrader. However, the events of interest populate in rather limited region of the outgoing K^+ angle (θ_{K^+}). This is because of the two-body kinematics in the $K^- p \rightarrow K^+ \Xi^-$ reaction which restrict the Ξ^- momentum at the entrance into the degrader and also because of the geometry of wedge degraders which minimizes the angular correction to the energy loss, as mentioned above. The simulation has shown that useful events populate mostly in the region of $5° \lesssim \theta_{K^+} \lesssim 9°$, and this helps to increase the fraction of Ξ^-'s stopping in LD_2 as indicated in Figure 9-b).

Another important technique for tagging of stopping Ξ^-'s is an energy loss measurement with the silicon detectors. A calculation shows that the kinetic energy of the Ξ^- at the entrance of a silicon pad must be lower than 30 MeV for stopping in the LD_2 vessel. This implies that the Ξ^-'s stopped in LD_2 leave large energy deposit in the silicon pad. Figure 10 shows the distribution of simulated energy loss ΔE_{SI} for Ξ^-'s stopping in LD_2, as well as that for all of the Ξ^-'s which hit the silicon pads. The energy deposit of interest is from 1.0 to 2.1 MeV. In Figure 9-c) are shown the stopping positions of Ξ^-'s tagged with $5° \lesssim \theta_{K^+} \lesssim 9°$ and $1.0 \lesssim \Delta E_{SI}$ (MeV) $\lesssim 2.1$. In Table 4 are summarized the results of the Monte Carlo simulation for the K^+'s in the angular region from 5° to 9°. As shown in the table, the fraction of Ξ^-'s stopping in LD_2 is 0.24% of the total created Ξ^-'s, while it is 15% of the events tagged with $1.0 \lesssim \Delta E_{SI} \lesssim 2.1$ MeV.

2.5 Neutron Detection System (ND, CV)

Neutrons were detected with two identical arrays of plastic scintillator logs placed

Table 4. Result of a Monte Carlo simulation for the Ξ^- decay or stop. A number represents percentage fraction of each category in the total events simulated in the region of $5° \lesssim \theta_{K^+} \lesssim 9°$. Results with the tag, $1.0 \lesssim \Delta E_{SI}$ (MeV)) $\lesssim 2.1$, are shown in the right column. A number in parenthesis represents percentage fraction of each category in the tagged events.

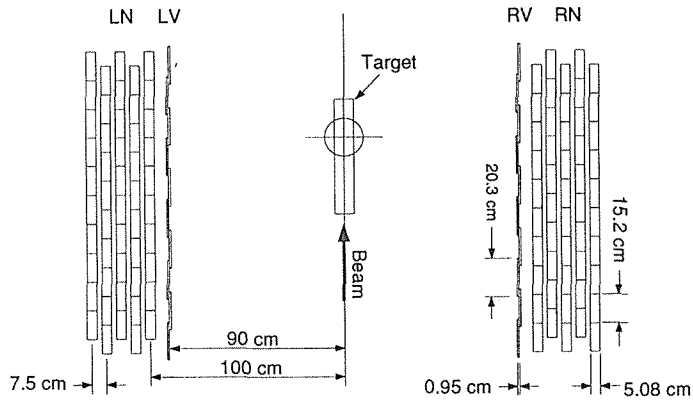|		$1.0 \lesssim \Delta E_{SI} \lesssim 2.1$
Ξ^- produced with $5° \lesssim \theta_{K^+} \lesssim 9°$	100.0	
Decay total	96.5	
Stop total	3.5	
- **Stop in** LD_2	**0.24**	
Decay before reaching SI	90.0	
Stop before reaching SI	2.45	
- Stop in aluminum	0.17	
- Stop in tungsten	2.28	
Hit SI	6.63	1.46 (100.0)
- Decay	5.58	1.10 (75.7)
- Stop in silicon	0.03	0.00 (0.17)
- Stop in aluminum (behind SI)	0.21	0.06 (3.90)
- **Stop in** LD_2	**0.24**	**0.22 (15.1)**
- Stop in the next degrader cell	0.56	0.07 (4.87)

Fig. 11.   Plan view of the neutron detector array ND.   The charged-particle veto
layer CV is also shown.

on the left side (LN) and the right side (RN) of the beam, as shown in Figure 11.   Each
array consisted of five layers which were staggered by 7.6 cm.   One layer was made up
of ten logs.   Each log was 15.2 cm wide, 182.9 cm long and 5.1 cm thick.   This
arrangement allowed the localization of the firing position to determine the flight length
which was necessary to calculate the velocity and the energy of the neutron from the
measured TOF.   Each end of the element was coupled to a PMT (Amperex 2262)
through a trapezoidal light guide.   Pulses from each PMT were discriminated by a
CFD (Phillips 715) and read with a Kinetic F432 TDC to give the timing information.
The threshold voltage applied to the discriminator input was 50 mV, corresponding to
the light output of about 0.25 MeV_{ee}[3].   The mean time of the two PMT signals gave the
neutron TOF, while their time difference gave the position of the interaction along the
log.   The front surfaces of the arrays LN and RN were about 1 m away from the target,
and the layers surrounded the target with solid angle of $0.21 \times 4\pi$ str.   The intrinsic
time resolution for minimum ionizing particles was measured to be 137 psec on average
for 100 logs by using cosmic rays.   The layers for charged particle veto (CV), made of
0.95 cm thick scintillators, were placed in front of each ND array for distinguishing hits
of neutrons from those of charged particles.

The neutron detection relies upon nuclear reactions which release charged
particles.   The efficiency of the neutron detection and its dependence on the neutron
kinetic energy have been studied with a Monte Carlo program which simulates the
neutron reactions in scintillator materials.   The simulation is based on the program
called "DEMONS" which has been developed for the purpose of estimating the
performance of multi-element neutron detectors [30, 31].   It has been reported that the
calculated efficiencies for the neutron detection agree with those of measurements
within 10%.   The code has a capability of estimating the loss of neutron flux due to
interactions in the layer for charged particle veto.   By adapting this code to the
geometry of the ND arrays and CV layers, we have estimated the detection probability
(η_{ND}), which is essentially the efficiency (ε_{ND}) times the solid angle ($\Delta\Omega_{ND}$), for

[3]   One MeV_{ee} or "MeV electron-equivalent" is the light output for electron energy deposit of 1 MeV.
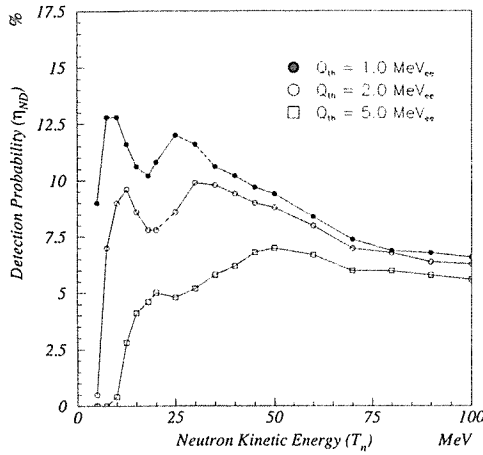
Fig. 12. Neutron detection probability η_{ND} estimated with the DEMONS program for the light output thresholds of 1, 2 and 5 MeV$_{ee}$.

neutrons emitted from the LD_2 vessel. Figure 12 shows the estimated η_{ND} as a function of the neutron kinetic energy with different threshold values for the light output.

2.6 Trigger

The event triggers were formed by using signals from the hodoscopes (IT, FP and BP), the Čerenkov counters (IC, FC, BC1 and BC2) and also the silicon detectors (SI). Triggers for $K^- p \rightarrow K^+ \Xi^-$ reactions were defined as:

$$KK = (IT \cap \overline{IC}) \cap (FP_1^{12} \cap BP \cap \overline{FP_{13}^{16}} \cap \overline{(FC \cup BC1)}) \tag{7}$$

$$KKL = KK \cap BC2 \tag{8}$$

$$KKS = KK \cap SI \tag{9}$$

$$KKLS = KK \cap BC2 \cap SI. \tag{10}$$

Here FP_1^{12} stands for the out-of-beam section of FP (modules #1–#12), while FP_{13}^{16} stands for the in-beam section of *FP* (modules #13–#16) which were used as a beam veto. The main trigger used in the 1992 run was the *KKLS* trigger which was the most efficient one for the Ξ^- stopping events. Data for the other triggers were taken concurrently with appropriate pre-scale factors. The rate for the *KK* trigger was typically 1500 per $10^6 K^-$'s incident on the target, while it was reduced to 190 for the *KKLS* trigger.

Further reduction of the trigger rate was achieved by rejecting proton events with the second-level trigger based on a front-end computer. The rejection was done based on the TOF difference between protons and kaons. The bottom half of the FD3 y-y' planes were segmented to give 16-bit information of vertical hit positions by which the momenta of outgoing particles were roughly determined combined with BT. Signals from BT were digitized by the LeCroy FERA/FERET system to provide fast information of hits. With this second-level trigger, the event rate was reduced to roughly 30 per $10^6 K^-$'s for the events triggered by *KKLS*, and the live time of data acquisition system was more than 80% of the total running time.

3. Data Evaluation

The present experiment for the H search is decomposed into three measurements i.e., 1) identification of Ξ^- produced in the reaction $K^- p \to K^+ \Xi^-$, 2) tagging of the stopping Ξ^-'s with the silicon detector and 3) neutron measurement in coincidence with the other two measurements. In this section, the performance of each measurement is evaluated based on the analysis of data collected in 1992.

In the 1992 run, the primary protons were delivered to the production target with a typical intensity of 4×10^{12}/spill. The total number of useful spills was about 3×10^5, corresponding to about 300 effective beam hours. The accumulated number of K^-'s on the target, N_{K^-}, was 2.73×10^{11}, while that of π^-'s was 7.99×10^{11}. Therefore, the average K^- intensity was 0.9×10^6/spill with π^-/K^- ratio of 2.9.

3.1 Identification of Ξ^- Production

The events involving outgoing K^+'s (K^+ events) have been extracted from the acquired data according to the results of particle identification. At the on-line stage, the fraction of K^+ events in the data is only about 1.4% even with the suppression of outgoing protons by the second-level trigger. The outgoing K^+ has been identified with the measured momentum and the time-of-flight. The method of track reconstruction is based on a first order transport theory. The transport matrices, which consist of partial derivatives of outgoing track parameters as functions of incoming track parameters, are prepared for each section of the spectrometer acceptance divided into 480. A track in a small region of phase space is approximated with a linear extrapolation from a central track in each section. A Monte Carlo simulation indicates that the error of the momentum obtained with this method is less than 0.3% of the true value. The time-of-flight has been obtained by using the averaged firing time of two output pulses from both ends of a BT log. Each BT log has been calibrated so that the measured TOF gives a correct timing for outgoing protons.

Figure 13 shows the reconstructed mass distribution for outgoing particles in the momentum region from 1.0 to 1.3 GeV/c, the region of interest for Ξ^- production. In this figure, it is required that the energy deposit on SI (ΔE_{SI}) is greater than 0.3 MeV (the analysis of the silicon detector is explained in Section 3.2). The K^+ is identified clearly in the mass spectrum. We have selected events in the mass region from 0.4 to 0.6 GeV/c^2. The contamination of misidentified pions or protons in the selected region has been evaluated to be less than 1% by extrapolating the tails of the peaks of pions or protons. The contamination of flat background underneath the K^+ peak, which is mainly due to in-flight decay and accidental hits, has been estimated to be 2%. Therefore, the total background contamination in the selected K^+ events has been evaluated to be 2~3%.

Figure 14 shows the missing mass spectrum for the identified events of $K^- + p \to K^+ + MM$ for which $\Delta E_{SI} \geq 0.3$ MeV is required. The peak resulting from the Ξ^- production appears clearly in the spectrum. The width of the peak is 15 MeV/c^2 (FWHM), corresponding to the momentum resolution, $\Delta p/p$, of 1% (FWHM). The final cut to select events of the Ξ^- production has been set to 1.28 GeV/$c^2 \leq MM \leq 1.42$
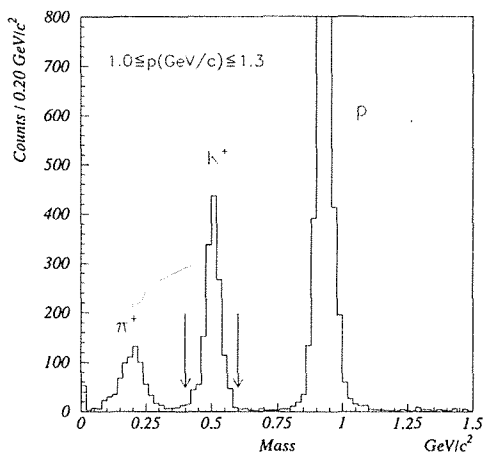
Fig. 13.   Mass spectrum of outgoing particles in the momentum region of $1.0 \leq p(\text{GeV}/c) \leq 1.3$. Arrows indicate the cut positions for selecting events.
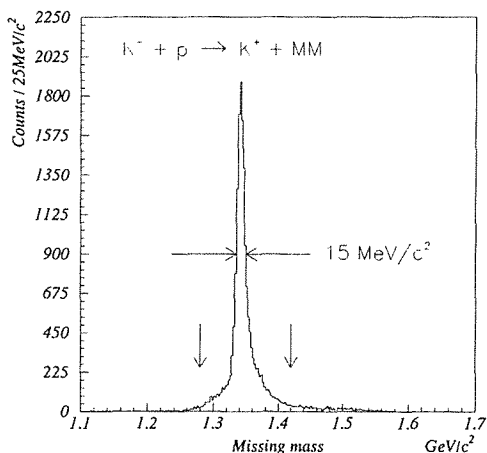
Fig. 14.   Missing mass spectrum for the reaction $K^- p \to K^+ MM$. Arrows indicate the selection criteria for the Ξ^- events.

GeV/c^2.   The tails of the peak arise mainly from reactions on other materials than LH_2 which still remain after vertex cuts are applied.   By comparing the data of the normal runs with data of empty-target runs, the contamination of such out-of-target reactions has been estimated to be 6% in the selected region.   Combining with the above mentioned background in the K^+ identification, background contamination in the selected events of the Ξ^- production has been evaluated to be about 8%.

The amount of Ξ^-'s identified in the 1992 data is approximately 1.5×10^5 in all the K^+ angular region and 5.0×10^4 in the angular region of K^+ from 5° to 9°, where most of events for the stopping Ξ^-'s populate.

3.2   Tagging of Stopping Ξ^-'s
3.2.1   Calibration of the Silicon Detector

The ADC information from each silicon pad is converted to an energy deposit ΔE_{SI} as :

$$\Delta E_{SI} = K_{SI} \times (q - q_0), \tag{11}$$

where q_0 is the pedestal to be subtracted from the raw ADC value q.   The energy resolution of the device evaluated from a pedestal peak width is 45 KeV (FWHM).

The gain parameter K_{SI} which gives an absolute energy scale for each pad has been calibrated with data of elastic scattering $K^- p \to p K^-$ taking account of the variation of the thickness of the silicon wafers[4].   As shown in Figure 15, K^- scattered elastically at a typical emission angle of 130° deposits the energy of about 0.3MeV on a silicon pad after losing its energy in the 0.137 cm (0.054″) thick aluminum interface between LH_2 and LD_2 and also the 0.051 cm (0.02″) thick aluminum wall between the pad and LD_2. In the calibration, first, the relative gain for each wafer is adjusted by comparing

---

[4]   The pad-by-pad variation, which is arisen from the difference in electronics such as pre-amplifiers and ADC's, is evaluated using a test signal put into the pre-amplifier.
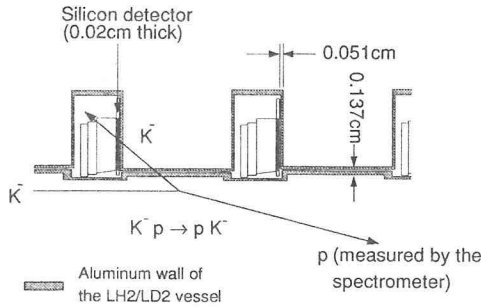
Fig. 15.   Drawing to show the method of
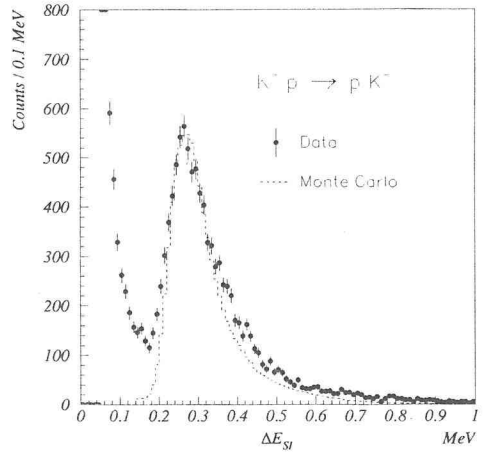calibrating SI with $K^-p \to pK^-$
elastic scattering.

Fig. 16.   Comparison of the measured spec-
trum of ΔE_{SI} (closed circles) with a
Monte Carlo simulation (dotted
line) for the $K^-p \to pK^-$ elastic
scattering events.

measured energy deposits with predicted values.   It is made on the event-by-event
basis by calculating the initial K^- momentum vector with the two-body kinematics
from the angle of the outgoing proton and by calculating the mean energy loss in the
aluminum material.   The accuracy of this adjustment is $\pm 10\%$, which is limited by
the number of events for each wafer (about 100 events per wafer).   Once this
adjustment is made, the overall energy scale ($\langle K_{SI} \rangle$) has been determined by comparing
the ΔE_{SI} spectrum measured for all pads to a Monte Carlo simulation.   Figure 16
shows a comparison between the data and the simulation after the calibration.   The
simulation includes the above mentioned $\pm 10\%$ error in the relative gain of wafers and
also the Vavilov-type straggling effect on the energy loss, which gives the peak energy
loss smaller than the mean energy loss in thin medium.   The agreement between the
data and the simulation is satisfactory.   It has been estimated that the accuracy of
$\langle K_{SI} \rangle$ is $\pm 2\%$($\pm 1\%$ for statistical error in the fitting of data to the simulated spectrum
and $\pm 1\%$ for ambiguity in the simulation).

3.2.2 Tagging Probability

The reconstructed events of the Ξ^- production have been further selected
according to the energy measured with the silicon detectors for tagging of Ξ^-'s stopped
in LD_2.   The response of the silicon detector to the identified $K^-p \to K^+\Xi^-$ reactions
has been compared to a Monte Carlo simulation for a verification of the tagging
technique with this device.   The simulation includes the contribution of pions and
protons stemming from the Ξ^- decay:

$$\Xi^- \to \Lambda\pi^- \text{ followed by } \Lambda \to \begin{cases} p\pi^- & (64.1\%) \\ n\pi^0 & (35.7\%) \end{cases} \tag{12}$$

These pions and protons induce false tagging signals which are misidentified as signals
of stopping Ξ^-'s, if they leave a large energy deposit on the silicon detector.   In the
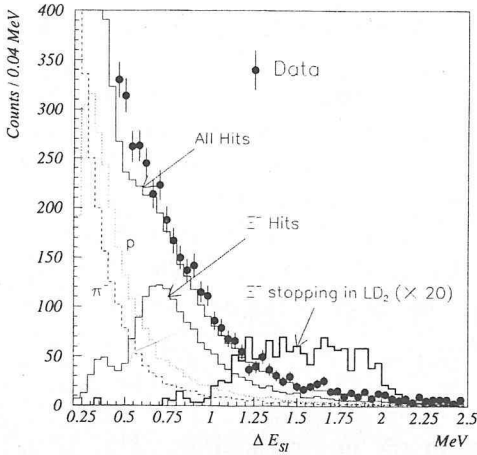
Fig. 17. Comparison of the measured energy deposit ΔE_{SI} (closed circles) to the simulation. Simulated spectrum for each component, Ξ^-, p and π^- from the Ξ^- decay, is also shown. Thick solid line shows the simulated ΔE_{SI} for Ξ^-'s stopping in LD_2, magnified by 20.
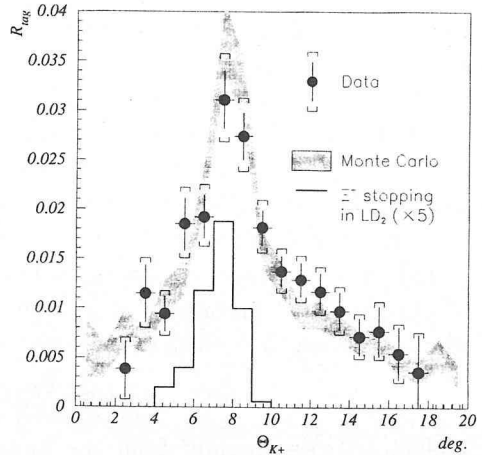
Fig. 18. Tagging probability R_{tag} as a function of θ_{K^+} obtained from the data (closed circles) and the Monte Carlo simulation (hatched band). The solid line indicates the contribution of Ξ^-'s which stop in LD_2 in the simulation (scaled by a factor of 5).

analysis, the position of a SI hit is checked against the two-body kinematics of the $K^- p \rightarrow K^+ \Xi^-$ process in order to minimize such background hits.

Figure 17 shows the measured ΔE_{SI} spectrum in the K^+ angular region of $5° \leq \theta_{K^+} \leq 9°$, which is compared to the simulation. The simulation indicates that hits of the daughter pions and protons are dominant in the low energy region and the Ξ^- component becomes significantly large above 0.6 MeV, where the data and the simulation are in good agreement. In Figure 18 is shown the tagging probability (R_{tag}), that is the fraction of Ξ^- events giving the tag in the region of $1.0 \leq \Delta E_{SI}$ (MeV) ≤ 2.1:

$$R_{tag} \equiv \frac{N_{tag}}{N_{\Xi^-}}, \tag{13}$$

as a function of the outgoing K^+ angle. Note that the data and the simulation are compared on the absolute scale. The vertical bars of the data represent the statistical errors, while the brackets indicate the ambiguity of the result ($\pm 5\%$) when the $\pm 2\%$ error in the absolute calibration of ΔE_{SI} (see Section 3.2.1) is taken into account. The tagging probability in the simulation is shown by a hatched band whose width includes the statistical error in the simulation and the systematic error due to an ambiguity in vertical positioning of the beam (1 mm)[5]. The solid line in Figure 18 shows the expected distribution for stopping Ξ^-'s in LD_2 which is magnified by a factor of 5. The θ_{K^+} dependence of R_{tag} has been understood with the peak around $\theta_{K^+} = 8°$

---

[5] A change of vertical positioning of the beam has a serious effect on the tagging probability because the flight length of a created Ξ^- changes rapidly with the beam height. The position of LH_2 and LD_2 vessels in an absolute coordinate could not be verified with an accuracy better than 1mm after the vessels were installed inside the vacuum container and were cooled down.

contributed by $\varXi^-$ hits and the tail caused by daughter protons and pions from the $\varXi^-$ decay.

As shown in these comparisons, the observed response of the silicon detector has been well understood by taking the contribution of daughter protons and pions from the $\varXi^-$ decay into account. The stopping probability of $\varXi^-$, which is 15% as shown in Table 4, is lowered because of the contribution of those daughter particles in the tagging. The simulation indicates that the contribution of $\varXi^-$ hits is 56% of the events tagged in the regions of $5° \leq \theta_{K^+} \leq 9°$ and $1.0 \leq \varDelta E_{SI}(\text{MeV}) \leq 2.1$. Therefore, the effective stopping probability η_{stop}, namely the ratio of $\varXi^-$'s stopping in LD_2 to the number of tagged events, is evaluated to be:

$$\eta_{stop} = 0.56 \times 0.15 \sim 0.086^{+0.004}_{-0.006}. \tag{14}$$

The error arises mainly from the ambiguity in the measured $\varDelta E_{SI}$. The $\pm 2\%$ ambiguity in the absolute calibration of $\varDelta E_{SI}$ leads to $\pm 5\%$ error in the estimate for η_{stop}. Another cause of the error is a possible decrease of the stopping power for $\varXi^-$ in the very low energy region, known as the Barkas effect. It has been reported for several materials that the stopping power for antiprotons is about one half of that for protons in the energy region below 1 MeV [32]. The possible decrease in the stopping probability has been evaluated to be about 5% by assuming the same effect for $\varXi^-$'s. In Eq. (14), we have included this error in the systematic error. In the 1992 data, 950 tagged events ($N_{tag} = 950$) have been obtained corrected by the 8% background contribution in the identification of $\varXi^-$'s (number of tagged event without the correction is 1029). Therefore, the expected number of $\varXi^-$'s stopped in LD_2 (N_{stop}) has been obtained as:

$$N_{stop} = N_{tag} \times \eta_{stop} = 82 \pm 9^{+4}_{-6}. \tag{15}$$

The first error is statistical and the second is associated with the above mentioned systematic error for the tagging efficiency η_{stop}.

3.3 Neutron Measurement

3.3.1 Neutron Spectrum

Figure 19 shows the inverse velocity spectra of neutrons (β_n^{-1}) for the events tagged in the regions of $1.0 \leq \varDelta E_{SI} (\text{MeV}) \leq 2.1$ and $5.0° \leq \theta_{K^+} \leq 9.0°$. These spectra are referred as "tagged spectra". The spectra are shown for three light output thresholds (Q_{th}) of 1.0, 2.0 and 5.0 MeV$_{ee}$. In the analysis, the calibrated time average of two output pulses from both ends of each log gives the neutron TOF relative to IT (TOF_n), while their difference gives the vertical hit position along the log (Y_n). The x and z hit positions (X_n and Z_n) are measured at the log center. Then the neutron velocity β_n is calculated as:

$$\beta_n = \frac{\sqrt{(X_n - X_i)^2 + (Y_n - Y_i)^2 + (Z_n - Z_i)^2}}{(TOF_n - \delta t_K - \delta t_\varXi) \cdot c}. \tag{16}$$

Here c denotes the light velocity and the neutron TOF is corrected by the beam traveling time from IT to the reaction vertex for the $\varXi^-$ production (δt_K) and also by the average stopping time of $\varXi^-$ ($\delta t_\varXi$) which is calculated to be 0.56 nsec with a Monte

Carlo simulation. The neutron path length is the length from the neutron emission point (X_i, Y_i, Z_i), which is assumed to be at the center of the LD_2 cell behind the firing silicon pad, to the hit position on ND. The light output of neutron hits (Q_n) is calculated by taking the geometrical mean of two ADC values. The ADC data of each log has been calibrated with pulse heights observed for cosmic rays traversing the log perpendicularly, for which the average energy loss through the 5 cm thick scintillator log is 10 MeV. When adjacent logs are fired with consistent firing locations along the logs, the hits are clusterized and treated as the hit of a single neutron. For such a clusterized hit, the TOF and the hit position are given by the log whose TOF is the minimum in the cluster (the fastest firing log), whereas the total light output is given by the sum of light outputs from individual logs. Hits of charged particles are removed by using the information of the charged particle veto layers (LV and RV).

3.3.2 Neutron TOF Resolution

If the *H* exists, we anticipate a peak of monoenergetic neutrons in the tagged spectra. The Gaussian peaks in each spectrum shown in Figure 19 represent the predicted signal widths for assumed binding energies of 50, 20, 0, -10 and -15 MeV in the case of $R = 1$. The intrinsic neutron TOF resolution (σ_T), which is crucial for the peak width, has been evaluated from the resolution measured with cosmic rays (137 psec on the average of 100 logs) by taking account of the light output difference between hits of minimum ionizing particles and those of neutrons. The light output distribution for neutron hits has been calculated with the DEMONS program, mentioned in Section 2. The resolution has been estimated assuming that the
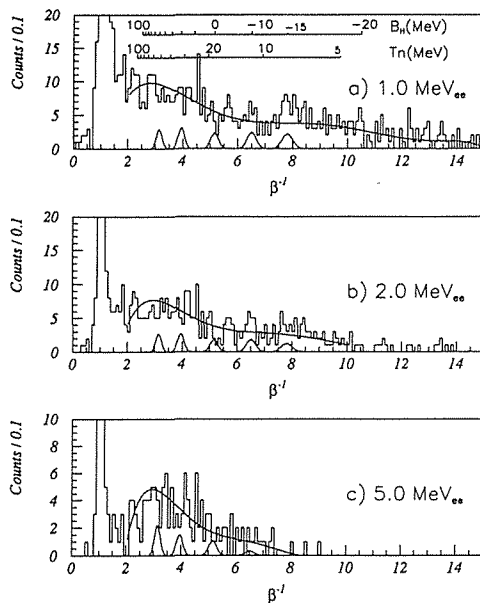

Fig. 19.   Tagged neutron β^{-1} spectrum for the light output threshold of a) 1.0, b) 2.0 and c) 5.0 MeV$_{ee}$. Gaussian peaks show the expected signal for assumed binding energies B_H of 50, 20, 0, -10 and -15 MeV and the branching ratio *R* of 1. Solid curve in each spectrum represents an estimated background.

dependence of the resolution on light output (Q) is expressed as $\sigma_T \propto 1/\sqrt{Q}$. Consequently, the intrinsic TOF resolution for neutron hits has been evaluated as a function of the neutron kinetic energies T_n in the form:

$$\sigma_T(T_n) = 560 \times [T_n(\text{MeV})]^{-0.281} \text{ psec.} \tag{17}$$

The signal shape in the spectrum of inverse velocity is then simulated with a Monte Carlo program which includes this evaluated TOF resolution as well as the effects of the path length ambiguity due to a finite thickness of a log (5 cm) and also the spread of Ξ^- stopping time (200 psec in FWHM). In Figure 20 is shown the peak width (σ_{peak}) predicted for several binding energies ranging from 100 to -18 MeV, corresponding to β^{-1} of 2.53 to 9.12. As indicated by the solid line, the β^{-1} dependence of the width can be parametrized as:

$$\sigma_{peak}(\beta^{-1}) = 0.0473 + 0.0186 \times \beta^{-1}. \tag{18}$$

3.3.3 Background Evaluation

The solid curve in each spectrum, shown in Figure 19, represents the estimated background in the region above the prominent peak at $\beta^{-1} = 1.0$ caused by hits of γ's. The neutron spectrum associated with Ξ^- production with a wider cut on ΔE_{SI} and without cut on θ_{K^+} is used to give an estimate of the background shape in the tagged spectrum. In Figure 21 are shown the neutron spectra obtained for the untagged Ξ^- events in the ΔE_{SI} region of $0.3 \leq \Delta E_{SI}(\text{MeV}) \leq 5.0$, and without cut on θ_{K^+} for the three light output threshold values. These spectra are referred as "untagged spectra". The
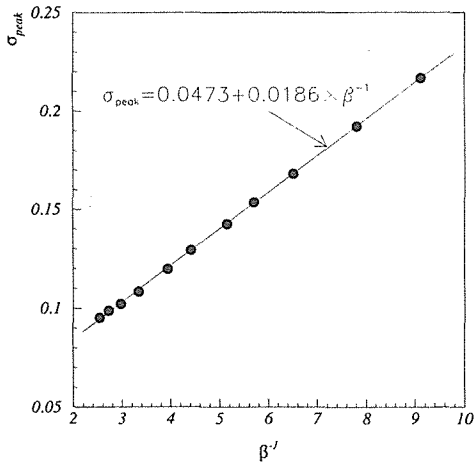
Fig. 20. Expected signal peak width σ_{peak} as a function of inverse velocity β^{-1} of the signal neutron.
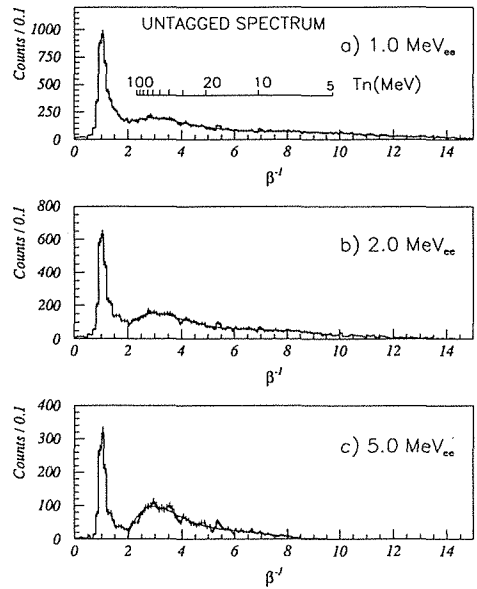
Fig. 21. Untagged neutron β^{-1} spectrum for the light output threshold of a) 1.0, b) 2.0 and c) 5.0 MeV$_{ee}$. Solid curve represents a sixth order polynomial fit to each spectrum.

solid curve in each spectrum represents a sixth-order polynomial to smooth the distribution of neutron hits. The smoothed spectrum is then scaled down to give an estimate of the background distribution in the tagged spectrum $f_{back}(\beta^{-1})$:

$$f_{back}(\beta^{-1}) = 0.95 \times \frac{N_{tag}}{N_{untag}} \times [\sum_{i=0}^{6} p_i \cdot (\beta^{-1})^i], \tag{19}$$

where p_i's stand for the coefficients of the above six-order polynomial. The scaling factor is taken to be the ratio of number of events found in the tagged and untagged data sets N_{tag}/N_{untag} with a correction factor of 0.95 which accounts for a small difference in the background rate between the tagged and untagged events. The effectiveness to use this scaled untagged spectrum as a background estimation has been assisted by a Monte Carlo simulation for the background. As discussed below, the background neutrons are mainly produced in capture processes of daughter π^-'s from Ξ^- decay. According to the simulation, the correction factor of 0.95 to the simple scaling is explained by a smaller fraction of Ξ^- decay and a consequent smaller stopping rate of pions in the tagged events compared to those in the untagged events. In the tagged events, the fraction of Ξ^-'s which are slow enough to stop in LD_2 or other materials before decaying in flight is enhanced. Moreover, the global agreement between the measured tagged spectrum and the scaled untagged spectrum $f_{back}(\beta^{-1})$ is good. When the smoothed untagged spectrum, $\sum_{i=0}^{6} p_i \cdot (\beta^{-1})^i$, is fit to the tagged spectrum, the reduced χ^2 evaluated in the β^{-1} region from 2.5 to 10.0 with a bin size of 0.2 is 0.68, 0.78 and 0.66 for $Q_{lh} = 1.0$, 2.0 and 5.0 MeV$_{ee}$, respectively. These small χ^2 values also indicate that the scaled untagged spectrum is a good approximation of the background.

The observed neutron spectrum has been compared to the simulation which includes neutron emission from π^--capture processes. In the simulation, the negative pions produced in the Ξ^- decay chain:

$$\Xi^- \to \Lambda \pi_\Xi^- \quad (100\%) \tag{20}$$

$$\Lambda \to P_\Lambda \pi_\Lambda^- \quad (64.1\%) \tag{21}$$

$$n_\Lambda \pi^0 \quad (35.7\%) \tag{22}$$

$$\pi^0 \to 2\gamma_\pi, \tag{23}$$

where particles in the final state are labeled by the mother particle species for convenience, are followed up in the area inside or surrounding the target. The simulation predicts that number of stopping pions per tagged event is 0.70 and 0.58 for π_Ξ^- and π_Λ^-, respectively. The stopping positions are found in material such as the degrader wedges, aluminum frame of the target structure, field clamp of the magnet and the neutron detector. The neutron yield from the π^--capture process has been reported in the literature [33] to be 1.7~1.8 per stopped π^- in the region of $T_n \geq 10$ MeV (direct neutrons), almost independent of the target mass number. Therefore, it is expected that the π^--capture process is a strong source of the background. If π^-'s stop, neutrons are generated with an isotropic angular distribution according to the reported yield and energy spectrum [33]. Figure 22 shows the comparison between the observed tagged spectrum and the simulated background for the three light output

threshold values (Q_{th}), where counts in each bin is normalized by the number of events for both the data and the Monte Carlo simulation.   It is noted that each data spectrum is shown by subtracting the flat distribution of accidental counts of which rate per event has been evaluated to be ~ 0.050, ~ 0.027 and ~ 0.008 for each β^{-1} bin of 0.25 for the thresholds of 1.0, 2.0 and 5.0 MeV$_{ee}$, respectively.   These rates of accidental counts have been evaluated from the counts existing below the prominent γ peak.   The simulation reproduces well the general shapes of the observed spectra.   In the case of 1.0-MeV$_{ee}$ threshold, the simulation accounts for about 70% of the observed rate in most of the β^{-1} region.   By raising up the light output thresholds, the agreement between the data and the simulation becomes better, as seen for the case of 5.0 MeV$_{ee}$ threshold.   Therefore, the neutron background has been qualitatively understood with the π^{-} capture processes originating from the $\varXi^{-}$ decay.

4   Search for the Signal

Based on the resolution and the background in the neutron detection, given by Eq. (18) and Eq. (19), respectively, the signal of the H formation has been searched for.   A narrow structure in the tagged spectrum would be an evidence of the final state neutron from the H formation $(\varXi^{-}, d)_{atom} \to Hn$.   If a bound H is produced, a monoenergetic neutron peak is expected to appear in the region of $\beta^{-1} \lesssim 5.2$ (bound region) with a
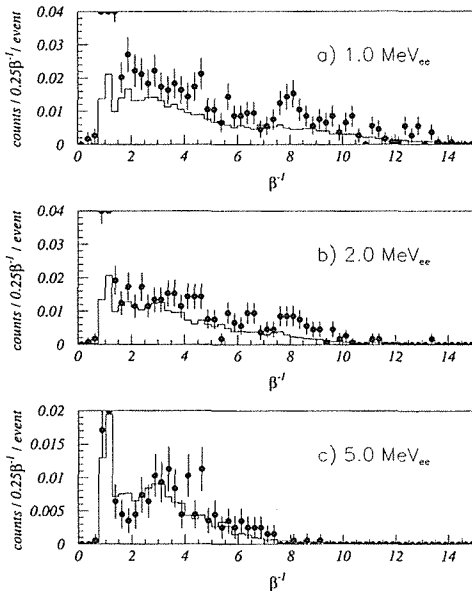

Fig. 22.   Comparison between the observed tagged spectra (closed circles) and the simulated background spectra (histogram) for the light output threshold of a) 1.0, b) 2.0 and c) 5.0 MeV$_{ee}$.
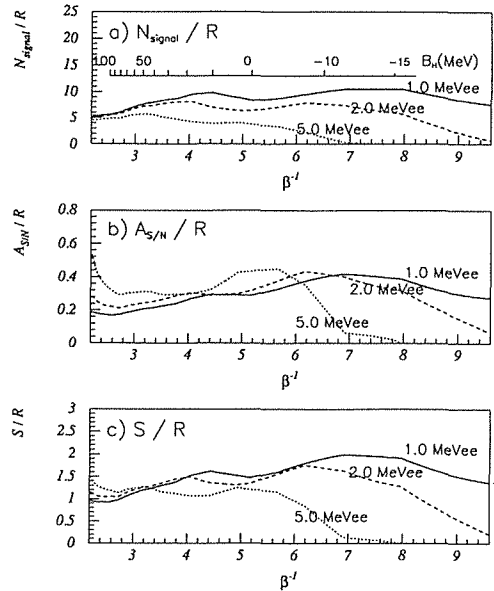
Fig. 23.   Expected performance of the signal search with the 1992 data: a) the expected yield of the signal neutrons N_{signal}, b) the ratio of signal to noise $A_{S/N}$ and c) the expected statistical significance of a peak S, normalized by R.

width consistent with the pure detector resolution. If the produced *H* is unbound, a bump is expected to be observed in the region of $\beta^{-1} \lesssim 5.2$ (unbound region) and the mass width Γ_m will be obtained from the bump width. If such a narrow structure is not found with enough significance, upper limits on the branching ratio *R* will be obtained for the $(\Xi^-, d)_{atom} \rightarrow Hn$ reaction. In this section, the results of the peak search and the upper limit deduction performed with the 1992 data are presented and discussed. The expected sensitivity to detect the signal is also shown. We have investigated in the region of β^{-1} from 3.0 to 9.6, corresponding to the binding energy (B_H) from 56 MeV $(m_H = 2175 \text{ MeV})$ to -19 MeV $(m_H = 2250 \text{ MeV})$, where the performance of the neutron detector has been studied and the employed method for the background subtraction is valid.

4.1 Expected Sensitivity

Figure 23 shows the expected performance of the signal search with the 1992 data : a) expected yield of the signal neutrons from the *H* formation (N_{signal}), b) the ratio of signal to noise $(A_{S/N})$ and c) the expected statistical significance of a peak (S). These three quantities are shown for $Q_{Jh} = 1.0$, 2.0 and 5.0 MeV$_{ee}$ with normalization to the branching ratio (R). The yield N_{signal} has been calculated from the expected number of Ξ^-'s stopped in LD_2 $(N_{stop}$, see Eq. (15)) as :

$$N_{signal} = N_{stop} \times \eta_{ND}(T_n) \times R, \tag{25}$$

where $\eta_{ND}(T_n)$ is the neutron detection probability evaluated with the DEMONS program (see Figure 12). As seen in the figure, about $10 \times R$ signal events are expected in the case of the light output threshold of 1.0 MeV$_{ee}$. The predicted signal peaks in Figure 19 are shown for the case of $R = 1$. The peak significance S is given as :

$$S \equiv \frac{n_{signal}}{\sqrt{n_{back}}} = A_{S/N} \times \sqrt{n_{back}} \tag{25}$$

$$A_{S/N} \equiv \frac{n_{signal}}{n_{back}}, \tag{26}$$

where n_{signal} is the number of expected signals in a small region of β^{-1} and n_{back} the background contribution underneath the peak. For evaluating n_{signal} and n_{back} at a given β^{-1}, a peak region with a width of $2\Delta\beta^{-1}$ is defined so that 90% of the Gaussian peak area is covered, i.e., :

$$\Delta\beta^{-1} = 1.64 \times \sigma_{peak}(\beta^{-1}) = 1.40 \times \Gamma_{HWHW}(\beta^{-1}). \tag{27}$$

Here $\sigma_{peak}(\beta^{-1})$ is the evaluated peak width in Eq. (19). The background n_{back} is calculated by integrating the background distribution $f_{back}(\beta^{-1})$, given by Eq. (19), in the same region. It must be mentioned that the quantities shown in Figure 23 are calculated assuming the zero mass width $(\Gamma_m = 0 \text{ MeV})$ for unbound *H*'s.

The results have revealed the dependence of the sensitivity for the signal detection on Q_{Jh}. If lower value of Q_{Jh} is taken, the sensitivity is higher in most of the region because of higher η_{ND}. Such a trend is more significant in the unbound region, where η_{ND} decreases rapidly by raising up Q_{Jh}. In contrast, the dependence of the sensitivity on Q_{Jh} is rather small in the bound region because of the weak Q_{Jh} dependence of η_{ND} in

the corresponding kinetic energy region (see Figure 12). Even higher sensitivity is expected with high Q_{Jh} values in the region of deep binding ($B_H \geq 60$ MeV), because the background decreases with Q_{Jh} more rapidly than the signal in this region. The rapid decrease of the background is due to low energy neutrons and γ-ray contamination in this region. According to the Monte Carlo simulation for π^- capture processes, discussed in Section 3, low energy neutrons produced by π^- captures which take place in ND is a cause of such background. Note that the hit of the π^- on CV is not effective to eliminate such background neutrons if their hits on ND are well isolated from the point of the π^- capture reaction.

4.2 Peak Search

Structures in the measured neutron spectrum have been examined by fitting the tagged spectrum with a bin size of 0.1 in β^{-1}, shown in Figure 19, with a Gaussian peak and the background f_{back} given by Eq. (19). In each step of the search, the position of a Gaussian peak is fixed at the center of a bin and the height (h) is taken as a fit parameter. The Gaussian width is fixed for the estimated peak width σ_{peak} given by Eq. (18) to search for a narrow structure. The fitting program is based on the CERN's MINUIT code and a log-likelihood technique is employed instead of the usual χ^2 method taking account of the low statistics of the data. Figure 24 shows the result of peak search in the tagged spectra with the three Q_{Jh}, that is 1.0, 2.0 and 5.0 MeV$_{ee}$. The peak height h at each point is plotted in unit of the standard deviation (σ), i.e., the height normalized to its error returned by the fitting routine ($h/\Delta h$).

The spectrum has a few bumps and dips. A fluctuation of 1 to 2 σ is usually treated as a pure statistical fluctuation of the background. In the bound region, no significant peak has been observed for all the values of Q_{Jh}. In the unbound region, a
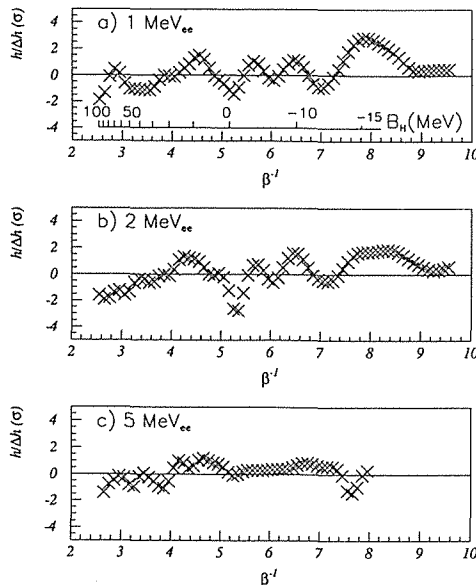

Fig. 24. Peak search result (in unit of σ) in the tagged spectrum for $Q_{Jh} =$ a) 1.0, b) 2.0 and c) 5.0 MeV$_{ee}$.

narrow bump of which statistical significance of the height $h/\Delta h$ is larger than 2.5 σ is seen at $\beta^{-1}=8.05$ with $Q_{lh}=1.0 \text{ MeV}_{ee}$. The Q_{lh} dependence of its significance seems to be consistent with the expectation shown in Figure 23-c). In the unbound region, however, the width of unbound states cannot be expected exactly. In this case, more appropriate way of evaluating the bump parameters and its significance is to take both the Gaussian height and its width as fit parameters. Such a two-parameter fitting has given this bump the height of 3.1 ± 1.2 (in a histogram with a bin size of 0.1 in β^{-1}) and a width of 0.35 ± 0.11 in β^{-1}. Consequently, the peak area has been calculated to be 27 ± 13. In the unbound H hypothesis, the measured centroid and width have given the mass of $m_H=2246 \text{ MeV}$ and the mass width of $\Gamma_m=1.9 \pm 0.9 \text{ MeV}$. The statistical significance of the bump has been evaluated to be 2.0σ from the measured peak area and its error. The value has not been statistically significant enough to establish the bump.

4.3 Upper Limit

The upper limit of the branching ratio R has been deduced from the observed number of events and the estimated background in the neutron spectrum with the method similar to the one described in Ref. [34, 35]. If the true value of the number of the signal events is μ_S, the probability of observing "n" events in a Poisson process is given by:

$$P(n)=\frac{e^{-(\mu_S+\mu_B)}(\mu_S+\mu_B)^n}{n!}, \tag{28}$$

where μ_B is the expected values of the background events. When "n_0" events have been observed in the experiment, in turn, the possibility that the true value of the number of the signal events is μ_S can be written as:

$$g(\mu_S)=N_1\frac{e^{-(\mu_S+\mu_B)}(\mu_S+\mu_B)^{n0}}{n_0!}, \tag{29}$$

where N_1 is the normalization constant such that:

$$\int_0^\infty g(\mu_S)d\mu_S=1. \tag{30}$$

The upper limit of μ_S at the confidence level of $(1-\alpha)\times 100\%$, denoted as $\overline{\mu_S}$, is given by:

$$1-\alpha=\int_{\overline{\mu_S}}^\infty g(\mu_S)d\mu_S. \tag{31}$$

When this method is applied for the estimation of the upper limit at a given β^{-1}, the observed number of events "n_0" and the expected background "μ_B" are obtained in the small region of β^{-1} with the width of $2\Delta\beta^{-1}$, as already introduced in Eq. (27) for evaluating the expected sensitivity. The region includes 90% of the signal events. Consequently, we obtain $\overline{\mu_S}$ in this region using Eq. (29)–(31). The number of the signal events in the region is calculated from N_{tag} as:

$$n_{signal}=0.9 \times N_{tag} \times \eta_{stop} \times \eta_{ND}(T_n) \times R. \tag{32}$$

Thus, the upper limit of R, denoted as $\overline{R}$, is obtained from $\overline{\mu_S}$ to be:

$$\overline{R}=\frac{\overline{\mu_S}}{0.9 \times N_{tag} \times \eta_{stop} \times \eta_{ND}(T_n)}. \tag{33}$$
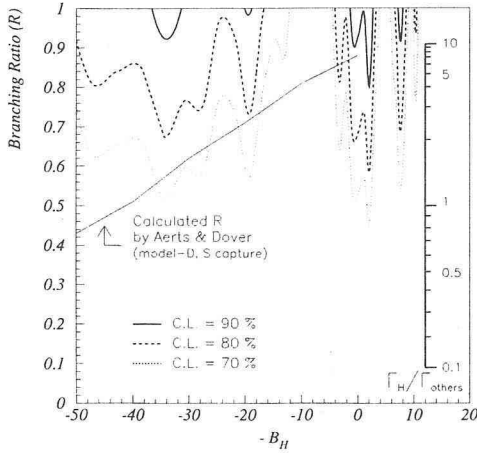
Fig. 25.   Upper limits on the branching ratio
           R at 90 (solid), 80 (dashed) and 70
           (dotted) % confidence levels. Thin
           solid line represents the prediction of
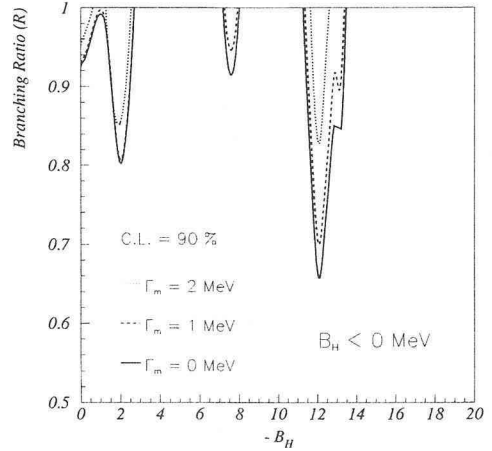   Aerts and Dover.

Fig. 26.   Upper limit on the branching ratio R
           (90% C.L.) for the unbound region
           ($B_H \leq 0$ MeV).   Assumed   mass
           widths Γ_m are 0 (solid), 1 (dashed)
           and 2 (dotted) MeV.

Figure 25 shows the upper limit of R for the region of the binding energy of H from 50 MeV to -19 MeV at the confidence levels of 90, 80 and 70%.   The result is based on the neutron spectrum with the light output threshold of 1.0 MeV$_{ee}$ where the expected sensitivity is higher for most of the β^{-1} region, as mentioned already.   For the unbound region, the upper limit has been obtained with assumed mass width Γ_m taking account of the decrease of the sensitivity due to broadening of the peak.   Figure 26 shows the obtained upper limits (90% C.L.) in the unbound region for assumed mass widths of 0, 1 and 2 MeV.

The solid line in Figure 25 represents the predicted R given by Aerts and Dover [25] for the Ξ^- capture from the S orbits.   In the calculation, the model-D of the Nijmegen potential is used to evaluate the fusion vertex of $\Xi^- p \rightarrow H$.   It is noted that the fraction of Ξ^- decay in the de-excitation process in the atomic orbits is neglected. The obtained upper limit on R provides information of the rate of the $(\Xi^-, d)_{atom} \rightarrow Hn$ process in relative to other processes.   In Figure 25, a scale is given for the ratio of the rate of the $(\Xi^-, d)_{atom} \rightarrow Hn$ process to that of the other processes, denoted as Γ_H/Γ_{others}, which is related to the branching ratio R as:

$$R = \frac{\Gamma_H/\Gamma_{others}}{\Gamma_H/\Gamma_{others} + 1}. \tag{34}$$

According to Aerts and Dover [25], the $(\Xi^-, d)_{atom} \rightarrow \Lambda\Lambda n$ process is the largest fraction in Γ_{others}.

The data shown here is not enough to answer definitely to the question of the existence or non-existence of the H because of the limited statistics.   Nevertheless, it must be emphasized that this formation experiment, where the sensitivity does not depend on the decay mode or the life time of the H, is advantageous to compare the experimental results with theoretical predictions in a less ambiguous manner than other types of measurements.   Assuming the same resolution for the signal and the same

ratio of signal to background evaluated in the present study, an upper limit on the branching ratio R will be as low as 0.5 (90% C.L.) with an accumulation of $10^{12} K^-$'s on target. By using the 2-GeV/c kaon beam line, whose performance is described in Section 2, this corresponds to less than 1000 hours of operation. It is expected that the upper limit on R is decreased in propotion to $1/\sqrt{N_{K^-}}$, where N_{K^-} is the accumulated number of the K^- beam. Therefore, further data taking with the same apparatus will provide an important information on the existence of the H particle.

5. Conclusion

The H particle search with the Ξ^- atomic-capture in liquid deuterium has been carried out for the first time. The method and the technique used in the experiment have been shown. In this experiment, the two successive reactions $K^- p \to K^+ \Xi^-$ and $(\Xi^-, d)_{atom} \to Hn$ have been studied. The Ξ^- production $K^- p \to K^+ \Xi^-$ is identified with the magnetic spectrometer. The stopping Ξ^-'s are tagged based on the energy loss which is measured with the silicon detector placed between the liquid hydrogen and deuterium vessels. The monoenergetic neutron signal from the H formation $(\Xi^-, d)_{atom} \to Hn$ is then searched for in coincidence with this tagging. It has been stressed that the usage of the 2-GeV/c beam line providing highly intense K^- beam of the order of 10^6/spill and the specialized target equipped with the silicon detector are essential to produce enough number of $(\Xi^-, d)_{atoms}$ with an improved tagging efficiency.

The analyses for the first available data collected in 1992 with 2.73×10^{11} K^-'s have been shown. The Ξ^- production $K^- p \to K^+ \Xi^-$ has been clearly identified in the missing mass of the reaction. Approximately 5.0×10^4 events have been obtained in the K^+ angular region from 5° to 9°, which is the region of interest for the stopping Ξ^-'s. The response of the silicon detector to the Ξ^- production events has been well understood with a Monte Carlos simulation. The number of Ξ^-'s stopped in liquid deuterium has been evaluated to be ~ 82. In the analysis of the neutron detection, evaluation of the resolution and the background rate are essential tasks. It has been shown that the observed neutron spectrum is largely populated by neutrons produced from the capture reactions of daughter π^-'s from the Ξ^- decay. The peak search has been performed on the tagged spectrum in the 1992 data for which about $10 \times R$ signal neutrons are expected. No significant peak has been seen in the spectrum. Calculated upper limits on the branching ratio R of the H formation reaction $(\Xi^-, d)_{atom} \to Hn$ have been presented. These results obtained from this first measurement have demonstrated that the present method based on the neutron detection with tagging of Ξ^- is an effective approach to search for the H and also to examine the H production rate from $(\Xi^-, d)_{atom}$.

for his continuous encouragement and helpful advice. I am indebted to them also for reading and correcting the manuscript.

The execution of the experiment described in this paper has been a combined effort of many individuals in the BNL-E813 collaboration. The collaborators in this experiment are : H. En'yo, K. Imai, A. Masaike from Kyoto University, K. Okada, F. Takeutchi from Kyoto Sangyo University, A.R. Berdoz, G.B. Franklin, R. Magahiz, C. Maher, F. Merrill, B. Quinn, R.A. Schumacher, I.R. Sukaton, V. Zeps from Carnegie Mellon University, R.E. Chrien, P.H. Pile, R. Sawafta, R. Sutter from Brookhaven National Laboratory, B. Bassalleck, A. Rusek, D.M. Wolfe from University of New Mexico, M. Burger, T. Bürger, H. Fischer, J. Franz, H. Schmitt, E. Rössle, M. Wieder from University of Freiburg, C.A. Davis, S.A. Page, W.D. Ramsay, V. Sum, W.T.H. van Oers from University of Manitoba, M. Athanas from University of California, San Diego, P.D. Barnes from Los Alamos National Laboratory, G.E. Diebold from Yale University, R.L. Stearns from Vassar College, J.J. Szymanski from Indiana University, D.R. Gill from TRIUMF, F.M. Rozon from University of Alberta, N. Hamann from CERN and J. Lowe, J.M. Nelson and R. Zybert from University of Birmingham. I would like to express my thanks to these peoples for their collaboration, many discussions and helpful advice for the experiment and the off-line analysis. It has been my great pleasure to work with them. In particular, I would like to express my thanks to the spokesmen of the experiment, Dr. P.D. Barnes and Prof. G.B. Franklin, for their support for my working on the experiment, valuable discussions and continuous encouragement. I wish to thank Prof. F. Takeutchi and Dr. R.E. Chrien for their support for my staying at Brookhaven.

I would like to acknowledge also the technical support of peoples at BNL who have played roles for the 2-GeV/c beam line and the cryogenic target which were essential for the execution of the experiment.

References

[1] R.L. Jaffe, *Phys. Rev. Lett.*, **38,** 195 (1977) ; **38,** 617 (1977) (E).
[2] A. Th. M.Aerts, P.J.G. Mulders and J.J. de Swart, *Phys. Rev.,* **D17,** 260 (1978).
[3] K.F. Liu and C.W. Wong, *Phys. Lett.,* **113B,** 1 (1982).
[4] P.J.G. Mulders and A.W. Thomas, *J.Phys. G: Nucl. Phys.,* **9,** 1159 (1983).
[5] B.O. Kerbikov, *Yad. Fiz.,* **39,** 816 (1984).
[6] M. Oka, K. Shimizu and K. Yazaki, *Nucl. Phys.,* **A464,** 700 (1987).
[7] B. Silvestre-Brac, J. Carbonell, and C. Gignoux, *Phys. Rev.,* **D36,** 2083 (1987).
[8] U. Straub, Z. Zhang, K. Bräuer, A. Faessler, S.B. Khadkikar and G. Lübeck, *Nucl. Phys.,* **A508,** 385c (1990).
[9] S. Takeuchi and M. Oka, *Phys. Rev. Lett.,* **66,** 1271 (1991).
[10] P.B. Mackenzie and H.B. Thacker, *Phys. Rev. Lett.,* **55,** 2539 (1985).
[11] Y. Iwasaki, T. Yoshié and Y. Tsuboi, *Phys. Rev. Lett.,* **60,** 1371 (1988).
[12] T. Yoshié, *Proc. of the Hadron '89 Conf.,* 365 (1989).
[13] A.S. Caroll et al., *Phys. Rev. Lett.,* **41,** 777 (1978).
[14] G.T. Condo et al., *Phys. Lett.,* **B144,** 27 (1984).
[15] H. Ejiri et al., *Phys. Lett.,* **B228,** 24 (1989).
[16] S. Aoki et al., *Phys. Rev. Lett.,* **65,** 1729 (1990).
[17] B. Shahbazian, A. Kechechyan, A. Tarasov and A. Martynov, *Z. Phys.,* **C39,** 151 (1988).
[18] B. Shahbazian, V. Sashin, A. Kechechyan and A. Martynov, *Phys. Lett.,* **B235,** 208 (1990).

[19] B. Shahbazian, T.A. Volokhovskaya, V.N. Yemelyanenko and A. Martynov, *Phys. Lett.,* **B316**, 593 (1993).

[20] K. Imai, *Nucl. Phys.,* **A527**, 181c (1991).

[21] M. Danysz et al., *Nucl. Phys.,* **49**, 121 (1963) and R. Dalitz et al., Proc. Royal Soc. Lond., **A426**, 1 (1989).

[22] D. Prowse, *Phys. Rev. Lett.,* **17**, 782 (1966).

[23] S. Aoki et al., *Prog. Theor. Phys.,* **85**, 1287 (1991).

[24] G.B. Franklin et al., AGS Research Proposal E813, BNL 1985, unpublished.

[25] A.T.M. Aerts and C.B. Dover, *Phys. Rev.,* **D29**, 433 (1984).

[26] G.B. Franklin et al., AGS Research Proposal E836, BNL 1986, unpublished.

[27] A.T.M. Aerts and C.B. Dover, *Phys. Rev.,* **D28**, 450 (1983).

[28] P.H. Pile et al., *Nucl. Instr. Meth.,* **A321**, 48 (1992).

[29] V. Sum et al., *Nucl. Instr. Meth.,* **A326**, 489 (1993).

[30] B.C. Byrd, P.L. McGaughcy, W.C. Sailor, R.C. Hammock and Y. Yariv, *Nucl. Instr. Meth.,* **A313**, 437 (1992).

[31] B.C. Byrd, W.C. Sailor, Y. Yariv, T.A. Carey and A. Gavron, *Nucl. Instr. Meth.,* **A313**, 457 (1992).

[32] R. Medenwaldt et al., *Nucl. Instr. Meth.,* **155**, 155 (1991).

[33] R. Madey et al., *Phys. Rev.,* **C25**, 3050 (1982).

[34] Review of Particle Properties, *Phys. Rev.,* **D45**, III-40 (1992).

[35] O. Helene, *Nucl. Instr. Meth.,* **A212**, 319 (1983).